© 2010 Oksen T Baris

THERMODYNAMIC MODELING AND MICROCALORIMETRY OF NANOSTRUCTURED MATERIALS FOR CAPACITIVE THERMAL MANAGEMENT OF ELECTRONICS

BY

OKSEN T BARIS

THESIS

Submitted in partial fulfillment of the requirements
for the degree of Master of Science in Mechanical Engineering
in the Graduate College of the
University of Illinois at Urbana-Champaign, 2010

Urbana, Illinois

Adviser:

Assistant Professor Sanjiv Sinha

ABSTRACT

Transient power dissipation profiles in handheld electronic devices alternate between high and low power states depending on usage. Capacitive thermal management based on phase change materials potentially offers a fan-less thermal management for such transient profiles. However, such capacitive management becomes feasible only if there is a significant enhancement in the enthalpy change per unit volume of the phase change material since existing bulk materials such as paraffin fall short of requirements. In this thesis I propose novel nanostructured thin-film materials that can potentially exhibit significantly enhanced volumetric enthalpy change. Using fundamental thermodynamics of phase transition, calculations regarding the enhancement resulting from superheating in such thin film systems is conducted. Furthermore design of a microfabricated calorimeter to measure such enhancements is explained in detail. This work advances the state-of-art of phase change materials for capacitive cooling of handheld devices.

This one is for my dear mom, dad and sister.

ACKNOWLEDGMENTS

I would like to use this page to thank everyone who made their contributions to this thesis by providing their support and wisdom. I would like to thank my Advisor Prof Sinha for his endless patience and willingness to help at all times. I am thankful for my Department, Mechanical Engineering and Science for their support. This work wouldn't be possible without contributions from my dear colleagues, and fellow group members Hongxiang, Jyothi, Marc and Junghyun. Special thanks should be attributed to Intel Research Council for funding my research.

TABLE OF CONTENTS

LIST OF FIGURES

LIST OF TABLES

CHAPTER 1

INTRODUCTION

The dramatic growth of handheld electronic devices arising from the confluence of telecommunication and information processing poses new challenges for thermal management. Passive thermal management such as in previous generation cellular phones limits higher power applications that are increasingly offered through smart phones. Low power consumption requirements render the use of existing cooling methods for microprocessors unattractive since they consume parasitic power through fans. Typically, handheld devices display transient power spikes followed by idle periods. Capacitive thermal management schemes can take advantage of such transients to deliver a fan-less solution. Capacitive cooling relies on heat storage in a thermally capacitive element during peak power spikes followed by heat release at a subsequent idle stage. The capacitive element is typically a phase change material (PCM). Table 1.1 lists the possible enthalpy change available through several fundamental processes that provide a relatively high change. All figures are based on water. Chemical bond formation and breakage ($\sim 10^{-18}$ J per molecule) and hydrogen bond breaking ($\sim 10^{-19}$ J per molecule) offer large changes in energy at the molecular level. However, these are typically not reversible without proper conditions and require too large an energy input. Compared to bond energies, the enthalpy of vaporization and fusion are two orders of magnitude smaller.The desired PCM properties for any application are high volumetric enthalpy change, a transition point within the operating temperature range of the device and reasonable thermal time constants for energy storage and relief.

Table 1.1: Magnitudes of molecular scale enthalpy change for fundamental processes involving water.

Type of Chemical Process	Magnitude (J) per Molecule
Valence Bond Breaking (Intramolecular)	$1x10^{-18}$
Hydrogen Bond Breaking(Intermolecular)	$1x10^{-19}$
Enthalpy of Vaporization	$6x10^{-20}$
Enthalpy of Melting	$1x10^{-20}$
Lattice Vibration	$1x10^{-21}$

Phase change occurs at a constant temperature without involving chemical reactions and is therefore, attractive for thermal energy storage. Amongst these, fusion involves a smaller volume change and is thus preferable provided it meets the storage capacity requirements. Phase change materials (PCMs) find usage in the thermal management of telecommunication batteries as well as energy storage in construction concrete[3, 4, 5]. The desired PCM properties for any application are high volumetric enthalpy change, a transition point within the operating temperature range of the device and reasonable thermal time constants for energy storage and relief.

Prior studies on phase change materials (PCMs) focus on large-scale applications [3]. Figure 1.1 shows thermal time constant per unit volume ($1m^3$) of several commonly used PCMs as a function of their volumetric enthalpy change. The time constants assume the length scale for heat conduction to be meters and the total volume to be $1m^3$. This is an oversimplification of the time constant for melting processes but provides a quick comparison. All materials included in the figure melt in the range of 300K-400K. The graph provides a snapshot of available materials and highlights the desired property regime. We derive the desired enthalpy change as follows. A typical handheld device consuming 10 W at peak usage yields a storage load of 145 kJ for a 4-hour usage period. For transient management of a handheld device of approximately 5x6x2.5 volume, the

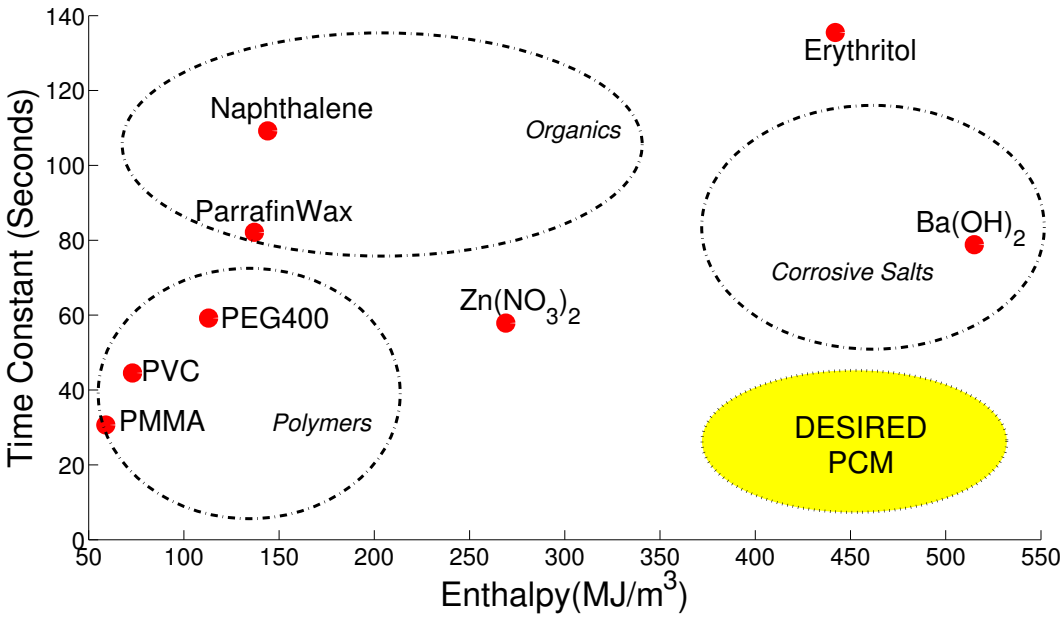

Figure 1.1: Thermal time constant vs volumetric enthalpy of melting for commonly used phase change materials (PCMs).

requirement is on the order of 2 GJ/m^3.

Along with such high volumetric capacity, a high thermal conductivity is also desirable for rapid regeneration of the PCM. Existing PCMs fail to satisfy the two disparate criteria. Based on Fig. 1.1, the use of paraffin for instance would require a volume of approximately 800cm^3 to maintain a 10W peak load system within the operating temperature. Use of PCM will be limited by its low thermal conductivity particularly in the liquid regime. Current PCM are hindered by the high thermal time constant and increased time required for diffusivity of the stored heat. Other materials whose properties are closer to the desired range are corrosive in nature and unsuitable for electronics cooling application.

There is a clear need to develop novel phase change materials that target the desired regime in terms of improved volumetric storage capacity. As a first step in this direction, this thesis presents fundamental theories based on thermodynamic arguments to consider interfacial modifications that enhance the enthalpy change

during phase transitions. The thesis covers a multi-layered nanostructured thin-film system of soft metals and explains calculation of the enthalpy change enhancement resulting from the reduced film dimensions. In the second part of the thesis a microscale calorimetry system is introduced to measure such thin film systems accurately and to verify the theoretical results.

CHAPTER 2

THEORY

2.1 Thermodynamic Modeling

Melting is defined as a phase transition in statistical physics. A system remains homogenous and stable as long as Gibbs equation and the stability criterion is satisfied. According to the stability criteria; any spontaneous process that follows variations in the equilibrium need to be working towards restoration of the system's equilibrium condition [6]. When the stability criteria explained above is not satisfied, the system breaks up into separate portions in other words the phase transition occurs. Melting is a particular type of first order phase transition phenomena between crystalline and liquid phases. First order transitions are characterized by discontinuities in the derivative of the free energy. These first order discontinuities give rise to high energy changes in comparison to second order transitions which arise from discontinuities in first order derivatives. Statistical thermodynamics uses the Gibbs relationship to define changes occurring between the solid and the liquid. The Gibbs free energy change, Δ G is:

$$\Delta G = H - T\Delta S = 0 \tag{2.1}$$

where H is enthalpy, T is temperature and ΔS is change in entropy. A phase transition may occur when the change in Gibbs free energy becomes zero. However, equilibrium or free energies of the phases alone do not explain when melting occurs.

Equally important is the thermodynamic mechanism by which the new phase first appears. This thermodynamic mechanism can be initiated by a nucleation in the bulk, near an impurity or at the surface [7]. The nucleation can be further tracked down to macromolecular structure. The macromolecular approach differs depending on rigidity of macromolecules. Rigid macromolecules have strong bonds that rarely break free. Small scale molecules on the other hand behave differently, such that their crystal structure is much weaker in comparison to rigid structures. Flexible molecule's features fall between rigid and small macromolecules [8]. Beyond macromolecular structure melting emerges as a microscopic transition. Several theoretical and semi-empirical models provide a microscopic description of melting [7]. Commonly these theories stem from packing considerations such as lattice instability or Born's theory of melting, whereby melting occurs when the shear modulus becomes zero [9]. Similarly there are well known theories by Lennard-Jones relating melting to spontaneous crystal lattice imperfections [10]. Another renowned theory is Lindemann's instability criterion[11]. According to this criterion, the vibration of atoms about their lattice sites keeps increasing in amplitude with temperature. Once the amplitude reaches a particular fraction of the nearest-neighbor distance, there is enough vibrational energy to disrupt the equilibrium crystal lattice and initiate the melting process. This simple criterion remains widely recognized today. Liang et al. [12] propose a Lindemann based model for interpreting size-dependent enthalpy and size-dependent melting point for nano-crystals embedded in a matrix. This energetic model is based on internal energy changes at the interfaces of the nano-particles with the matrix. The model predicts that the enthalpy of melting, H and the melting temperature, T are functions of the diameter of the particle or half thickness of the film structure,

denoted by D. Thus,

$$H(D) = H_0 + \Delta H = H_0 + (\Delta H_L - \Delta H_C) \tag{2.2}$$

where the subscripts *0, L and C* stand for the bulk crystal, the liquid and the nanocrystals respectively. Using an Al matrix with embedded Pb nanocrystals, *H(D)* and *T(D)* are observed to increase with decreasing size as long as $\Delta H > 0$; change in enthalpy of the nanocrystals exceeds that of the corresponding bulk crystals. This is summarized in the following equation which related the changed enthalpy to the original value as

$$\frac{H(D)}{H_0} = 1 + \left(\frac{D_c}{D}\right) \frac{\left(3(1 - \frac{U_L}{U_N})(U_M - U_N) + (U_M + U_N)\frac{(h_N^2 - h_M^2)}{h_M^2}\right)}{(24H_0)} \tag{2.3}$$

where $D_c$denotes critical size assuming almost all atoms of the nano-crystal are located on the surface, U denotes the molar cohesion energy, h is the atomic diameter, subscripts *M, N, L* correspond to matrix, nano-crystals and liquid respectively. This model successfully predicts changes in the melting enthalpy and the melting point. The change in enthalpy starts sub 100nm and increases dramatically for thicknesses less than 20nm. The model's application on In/Al and Pb/Al yields almost a twofold increase of the melting enthalpy. Nanda et al [13] repeated the measurements using the same matrix and observed the same increasing trend for melting temperature. Empirical model results analogous to Nanda and Liang illustrate that the melting nucleation originates at the microscopic structure of the interface between the coexisting phases. The phenomenon that explains this situation is called surface melting. During the surface melting stage bulk material still exists as a solid phase. While the surface of the material due to its lower coordination has already started the phase transition into liquid, the bulk material

exists as a stable solid phase [14]. Multitude of existing experimental and theoretical studies display direct evidences of surface melting using high energy proton beam scattering experiments [7]. Melting at the surface tends to start at a lower point than the bulk and more layers from the surface start to melt while approaching bulk melting point. Surface melting can give us an edge in terms altering melting behavior such that different material coatings can induce or hinder melting. Studies on GaAs and Ge show that surface effects can trigger melting for GaAs layers that would otherwise be stable. The perturbation relationship is explained by an increase in diffusion constant of the material that induces motion in the underlying layers [14]. The equation that governs the diffusion constant D_j is given as follows:

$$\left\langle \Delta R^2 \right\rangle_j (t) = 4 D_j t \tag{2.4}$$

Where diffusion mean square displacement $< \Delta R^2 >_j$ is an average over ions and t represents time. At the atomic level individual particles break away from surface layer to jump into the layer underneath and return within 1ps. These movements nucleate local disorder within the stable layer and induce melting such that Ge layer has introduced a diffusion coefficient of 10 on a GaAs layer that is otherwise stable. Surface induced melting is part of a larger statistical surface melting theory proposed by Lipowsky et al [15]. This critical surface behavior can be characterized by continuous changes on the surface whereas the bulk exhibits discontinuous changes during the transition. Using theories set forth through Lindemann's criterion, Liang's model and surface melting phenomenon we suggest a PCM structure for enhancement of the enthalpy of melting. The key to enhancing this enthalpy is confining surfaces to increase binding energy at the interface of coexisting phases. In a free standing surface the number of nearest atoms at the surface is small in comparison to bulk. This leads to faster disorder at the surface

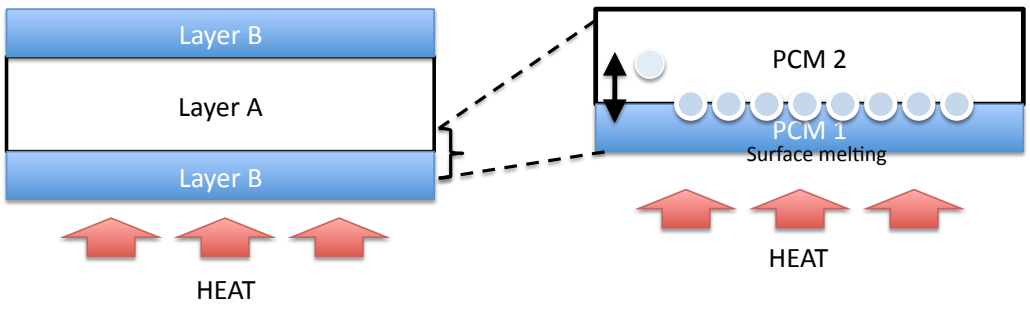

Figure 2.1: Stacked PCM model where we confine top and bottom surfaces of the PCM using a second layer, Surface induced melting, atoms jumping between layers start disorder in the second PCM layer

and initiates melting. By introducing a new layer and confining the surface we can increase the available number of atoms at the surface and induce a change in the melting behavior. Figure 2.1 illustrates the stacked PCM model. This model takes advantage of increased binding energy through confined free surfaces on both sides. Figure 2.1 shows how in a stacked layer structure, diffusion occurs by advent of jumping atoms from one layer to another. Figure 1a uses a three layer PCM model such that the Layer A is encapsulated by Layer B from top and bottom. This encapsulation confines both surfaces and alters the melting behavior due to theoretical reasons explained in the earlier paragraphs. Quantitative changes in the enthalpy of melting for the stacked model in figure 2.1 can be traced by applying equation 2.3 into different PCMs. The resulting melting enthalpy curves are illustrated in the next section.

2.2 Results

2.2.1 Polymers

Theoretical roots of enthalpy increase associated with confined surfaces can be traced through infinitely thick lamellar model[16]. Surfaces are well known to lower energy barriers and decrease enthalpy as a function of surface energy. The surface effect on the total enthalpy of melting is inversely proportional to fold length favoring extended chains. The relationship can be summarized by:

$$\Delta H_{Melting} = N_u \Delta H_{Melting,u} - 2\Delta H_\sigma = N_u \Delta H_{Melting,u} - 2(\frac{\sigma_e}{L_f}) \tag{2.5}$$

where N denotes infinitely long chains, u represents monomeric units and $\Delta H\sigma$ the surface enthalpy of the folds where σ_e stands for surface energy and L_f for fold length. Quantitative changes in the enthalpy of melting for the stacked model in figure 2.1 can be traced by applying equation 2.3 into different PCMs. The resulting melting enthalpy curves are illustrated using figure 2.2. Figure 2.2 uses three different encapsulation scenarios: Polypropylene sandwiched between Polystyrene(PS), Poly(methyl methacrylate) (PMMA) sandwiched between PS and a theoretical curve. PMMA encapsulated by PS shows small changes in the enthalpy of melting, only an increase with a factor of 1.25. The small increase is due to two materials having similar molecular diameters and cohesion energies. Polypropylene encapsulated by PS displays a 2.5 factor increase due to slight differences in material properties. Third curve is a theoretical curve that displays how changing the Radius of Gyration, RG ratio between the two materials can impact the enthalpy of melting with a factor of 10. The melting behavior in the nano-scale has a lot of uncertainty and conflicting theoretical models. Based on recent advancements and promising computational models we introduced a stacked PCM

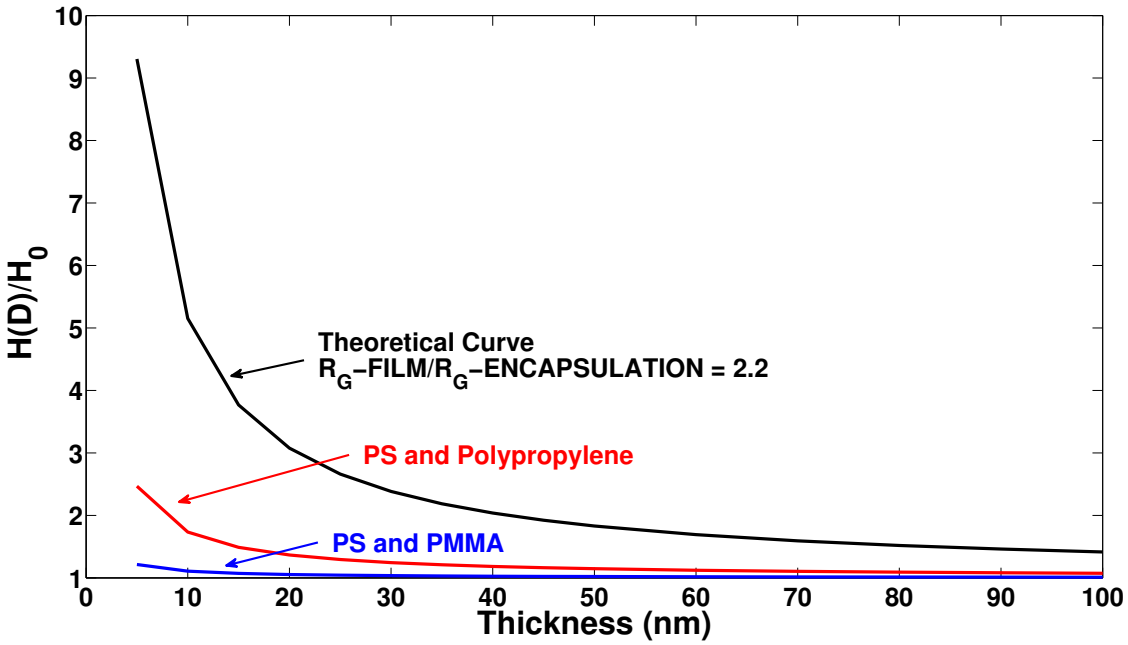

Figure 2.2: Preliminary PCM Encapsulation Scenarios

film model that can enhance the enthalpy of melting. In order to experimentally test the proposed model we need to carry out calorimetric measurements. Details of the experimental device and setup will be covered in the next section.

2.2.2 Metals

Superheating

The phenomenon of superheating describes an elevation in melting temperature. Superheating in nano-structures can be achieved using crystals with negative surface curvature [17], by drawing polymers [18], and by limiting the solid/liquid interface kinetics. Among these methods, embedding crystal particles epitaxially in another material has been theoretically and experimentally studied in greater detail [12]. The level of superheating is a function of particle diameter and increases for

decreasing particle size. Particles embedded in a matrix can be superheated above their bulk melting point by suppressing free surfaces at the matrix-crystal interface. Experimentally this can be achieved using sputtering technique to deposit layers with cohesive interfaces [19]. The resulting degree of superheating can reach up to 100K for Al/Pb matrix in the sub-10nm regime [19]. The increase is only apparent for nano-structures because the coating layer hinders the motion of nearby atomic layers and the superheating effect ceases for bulk structures. The degree of superheating can be expressed as a function of surface energy and then be used to interpret the increase in enthalpy. Following Nandas[13] particle model and Guisbers[20] enthalpy relationship we can quantify potential increments for viable materials. Cohesive energy is the key variable that affects the degree of superheating. Total cohesive energy for a nanoparticle of N atoms is:

$$E_b = a_v N - 4\pi r_a^2 N^{2/3}\gamma \tag{2.6}$$

where E is energy, a is cohesive energy, and γ is surface energy. The first term describes volume energy and the second term describes the surface energy component. N, number of atoms can be rewritten as $N = d^3/(2r_a)^3$. Dividing equation Eq. 2.6 by the number of atoms we can obtain cohesive energy per atom as a function of the surface energy, the atomic volume and the particle diameter:

$$a_{v,d} = a_v - \frac{6v_0\gamma}{d} \tag{2.7}$$

Cohesive energy values have been empirically determined based on empirical melting temperature data[13]. Introduction of an empirical relationship modifies

Eq. 2.7 to yield the change in melting temperature to be

$$\frac{T_M}{T_{M,b}} = 1 - \frac{6v_0\gamma}{0.0005736T_{m,b}}\frac{1}{d} = 1 - \frac{\beta}{d} = 1 - \frac{\beta}{6}\delta \tag{2.8}$$

where β is estimated using v_0, γ and T_m, b The shape factor, δ, is defined using the surface area to volume ratio. The shape factor for spherical particles is 6/d, for thin wires is 4/d, and for thin films is $\delta = 2/t$. Figure 2.3 plots the effect of the shape factor on the degree of superheating for In coated with Al. From a fundamental perspective altering the surface can theoretically increase or decrease the energy barrier at surface and hinder melting mobility of the particles at the surface. In the spherical particle case, the structure consists of crystal particles and surrounding matrix. The particles are completely saturated with the atoms of the surrounding matrix. Surface energy at the interface is changed such that the surface energy of the matrix will be introduced along with a correlation constant defining the level of cohesiveness between particles and the matrix:

$$a_{v,d} = a_v - \frac{6v_0(\gamma - \alpha\gamma_M)}{d} \tag{2.9}$$

The constant, α is 0 for free particles and 1 for perfect epitaxial layer between matrix and the particles. Following equations 2.8 and 2.9 results in superheating temperature relationship:

$$\frac{T_M}{T_{M,b}} = 1 - \frac{\beta}{d}\left(1 - \frac{\gamma_M}{\gamma}\right) = 1 - \frac{\beta}{6}\delta\left(1 - \frac{\gamma_M}{\gamma}\right) \tag{2.10}$$

where the degree of superheating is expressed as function of surface energy, particle diameter and empirical material constant beta. Taking advantage of the theory we can quantify possible increase for low melting point materials such as Gallium(302K) and Indium(430K).

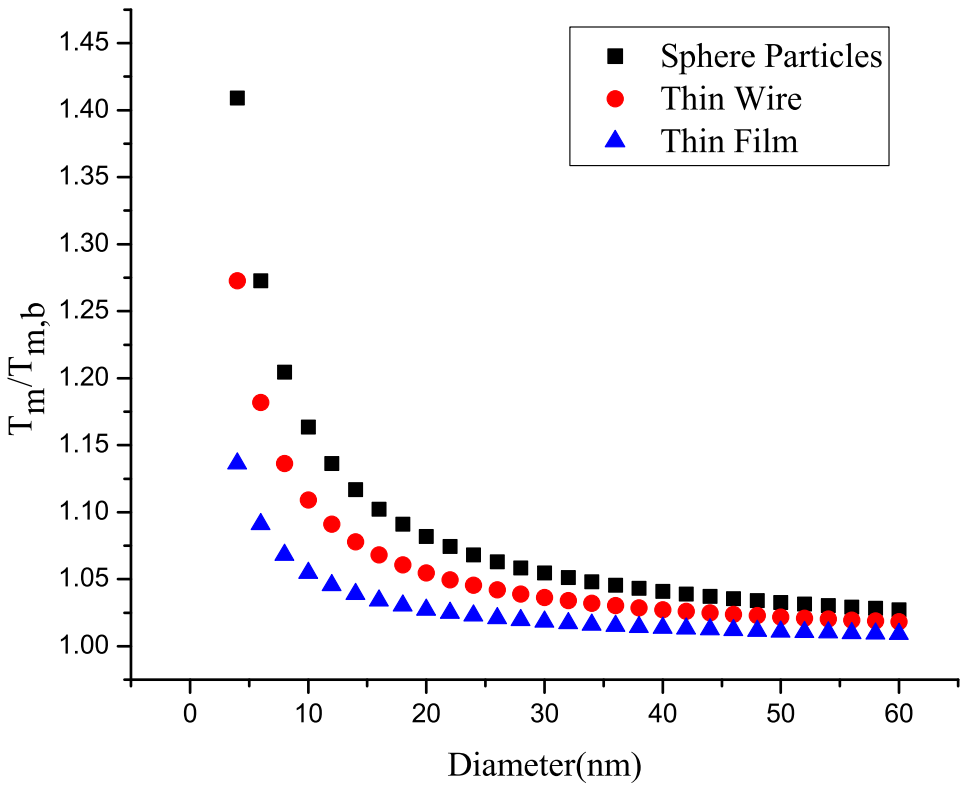

Figure 2.3: Degree of superheating vs diameter of spherical particles, thin wires and thin films(thickness)

Enthalpy Change

In this section, we derive the relationship between the degree of superheating and the melting enthalpy once again from using fundamental thermodynamic relations. We follow Guisbers freestanding particle derivation [11] and modify it for particles embedded in a matrix. Thermodynamic laws state that during phase transition the Gibbs free energy difference between the solid and the liquid states becomes zero. The Gibbs free energy of a nanostructure is considered to consist of two parts, the

bulk free energy and the surface energy. The total free energy for a state is

$$G = G_b + (A/V)\gamma \tag{2.11}$$

where G, is for Gibbs free energy, A surface area, V volume. The difference in Gibbs free energy can now be written as:

$$G_l - G_s = G_{l,b} - G_{s,b} + (A/V)(\gamma_l - \gamma_s) \tag{2.12}$$

where subscripts *l, s* and *b* denote liquid, solid and bulk respectively. Substituting *G=H-TS* yields Eq.2.11 in the following form:

$$\Delta H_M - T\Delta S_M = \Delta H_{M,b} - T\Delta S_{M,b} + (A/V)(\gamma_l - \gamma_s) \tag{2.13}$$

If the nanoparticles are embedded in a matrix, the surface energy term will be modified. Using the cohesion constant $\gamma s^* = \gamma_s - \alpha_l$, and rearranging Eq. 2.12, we get

$$\Delta H_M - T\Delta S_M = \Delta H_{M,b} - T\Delta S_{M,b} + (A/V)(\gamma_l^* - \gamma_s^*) \tag{2.14}$$

At the superheating limit, the particle begins to melt and the change in the Gibbs free energy becomes zero. Dividing Eq. 2.14 by the change in enthalpy in the bulk material, we get

$$\frac{T_M}{T_{M,b}} = 1 + (A/V)(\gamma_l^* - \gamma_s^*)\frac{1}{\Delta H_{M,b}} \tag{2.15}$$

If we substitute the bulk melting temperature, $\Delta H_{m,b} = T_{m,b}\Delta S_{m,b} = 0$,Eq.2.15 becomes

$$\Delta H_M - T_{M,b}\Delta S_M = 1 + (A/V)(\gamma_l^* - \gamma_s^*) \tag{2.16}$$

Finally combining the above two equations provides the relationship between temperature change and enthalpy change:

$$\frac{\Delta H_M}{\Delta H_{M,b}} = \frac{T_M}{T_{M,b}} \tag{2.17}$$

The linear relationship between enthalpy and temperature implies an increase in capacitive storage. Using results of Eq2.10 in combination with Eq 2.17 we can obtain the change in enthalpy and graph in figure2.4. Figure 2.4a displays degree of superheating and change in enthalpy for Gallium that can be maximized up to twice its melting point for particles of 10nm and less. Similarly an increase for Indium can account for twofold increase with small diameter particles. For both Indium and Gallium the enthalpy change is maximum when the coating is Platinum or Iron. The increase in enthalpy becomes apparent in 5nm for both materials. The increase is nonlinear and depends highly on the particle diameter in the sub 10nm range. In order to get 100% increase we need 5nm systems of which many layers need to be stacked to handle current thermal load demands. The linear relationship

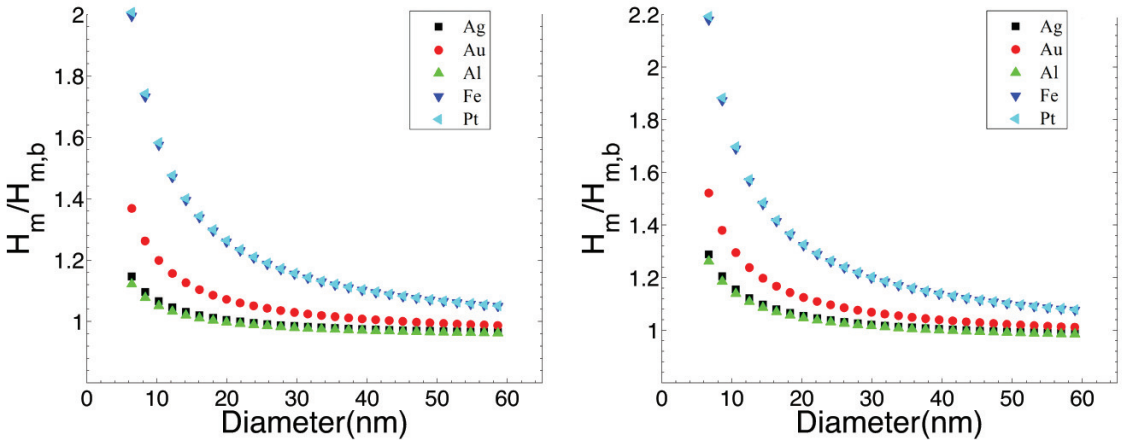

(a) Gallium (b) Indium

Figure 2.4: Degree of superheating and enthalpy increase for Ga(a) and In(b) particles embedded in high melting point metals

between temperature and enthalpy needs to be controlled carefully for application in the field. Expected enhancement on melting enthalpy and temperature of Ga is on the order of x1.5 and this will place Ga in comparison with high melting point materials. Upon enhancement enthalpy of Ga(Tm=303K) needs to be compared to high Tm materials such as Li(Tm=453.8K). Such a comparison yields that melting enthalpy of Ga($474MJ/m^3$) and its enhancement(711MJ/m^3) will surpass enthalpy of Li($228MJ/m63$). As shown by Eq.2.17, a significant degree of superheating can lead to an increase in the the melting enthalpy. However, the relation remains linear and is the key limitation of this method. Based on the above theory, superheating of thin film low melting point metals such as Gallium or Indium can potentially double their volumetric enthalpy of melting. While this increase is only 20% of the tenfold increase required from strict volume restrictions, it is nevertheless promising since other avenues for further enhancement may be possible. However, the above theory needs experimental verification before other avenues are considered. We describe below an experimental structure that can probe such enthalpy change enhancements in thin film systems.

CHAPTER 3

MICROCALORIMETRY

3.1 Differential Scanning Calorimetry

The phase transition and enthalpy enhancement theory discussed above need experimental verification. A microfabricated test structure is fabricated for conducting such measurements. The proposed setup consists of a temperature sensing calorimetry device to measure temperature, heat capacity and enthalpy of phase transitions. Calorimetry has been the prominent technique for measurement of heat changes occurring during a process. The means of achieving this measurement is the temperature. This century old classic technique has evolved into a new form called differential scanning calorimetry(DSC). Differential scanning calorimetry differs from calorimetry in the traditional sense by addition of a reference. DSC measures heat flow rate to the sample and the reference simultaneously, a differential analysis of the two results in a high sensitivity measurement of the exact heat flow and temperature increase in the sample. The reference is used to minimize the ambient uncertainties that are inherent to calorimetry technique. Advanced DSC equipment is capable of making sensitive measurements in miniscule sample sizes. In order to measure samples in the nano scale conventional DSC needs to be scaled down as well. DSC uses two simultaneous comparative measurements extracting relevant information from the difference between a sample and a reference. The reference provides an accurate baseline particularly in the nanoscale regime where the sample size and the heat capacity are

small in comparison to the measuring device. In order to accurately characterize increments in the proposed thin films, a device with a sensitivity on the order of 1 nJ is required. Commercial DSC equipment such as the TA Instruments Q2000 is suitable for μW sensitivity measurements[21]. The focus of our study is nanometer thick layers which require pW sensitivity in the nanogram regime. Thus, the measurements are outside the limits of a standard DSC device. Nano-calorimetry technique roots back to early 80's when first small sample calorimetry studies were done by Early et al [22], who introduced the idea of calorimeter in the micro scale. Nano-Calorimetry evolved in parallel to micro-fabricaton techniques and in 1994 Denlinger et al [23] developed the thin film micro-calorimeter technique. Denlinger's basic design consisted of a metal heater on a freestanding membrane structure. The nano-calorimeter design has not changed too much since then. Allen group at University of Illinois has developed an ultra-fast technique by simplifying the design and further refining the sensitivity [24]. The Allen design has been utilizing the scanning technique at ultra-fast heating rates(30000 K/sec) [25]. Fast scanning rates prevent heat dissipation by conducting experiments within 5-10ms time range. Recent advancements demonstrate that attojoule/kelvin resolution can be attained using an improved architecture comprising a smaller membrane isolated with a bridge type structure[26]. In this thesis we build upon previous joule heater type designs and develop a calorimeter to measure heat capacity of PCMs. The proposed design provides improved thermal isolation by minimizing heat loss from the metal heater. The materials of focus will be dielectric and therefore I utilized the use of metal surface for minimum heat loss through the freestanding membrane. Dielectric nature of the sample materials allow direct deposition of the sample on the heater without any intermediate electrical insulators. This reduces the amount of intermediate thermal resistances between the sample and the heater. The absence of insulation further decreases the total capacitance by reducing available thermal

mass. These refinements provide added sensitivity for the current design. Figure 3.1 provides an overview of the calorimeter structure. As illustrated in the graph the reference and sample measurements are done side by side simultaneously. The design will be used inside a vacuum chamber to maximize isolation. The fabrication of this design uses widely available micro-fabrication techniques. Silicon nitride layer is grown 100nm thick for maximum strength with minimum thermal mass. Metal and sample layers in consideration are both 50nm thick. The design goal of the calorimeter was to minimize the heat dissipation to internal components and ambient. In order to minimize the internal components a resistance and capacitance analysis has been carried out.

3.2 Design

Design of microcalorimeter is based on previous works by Allen et al[27], Hellman et al[23], both designs take advantage of minimizing the added thermal mass of the device. It is possible to increase the sensitivity of calorimetry measurement by taking advantage of mems fabrication techniques. An overview of the device and various layers used are displayed in figure 3.1.

3.2.1 Steady State Analysis

Steady state analysis is used to evaluate the differential scanning calorimeter design. Heat dissipation analysis results show that the calorimeter design is utilized for minimum heat loss through ambient and calorimeter itself. The heat dissipation paths are displayed schematically in figure 3.2. In this analysis we follow simplified resistance network to trace heat flow path throughout the device. In this design the aim is minimization of heat loss through contact resistances and losses to the ambient. In order to get a better understanding of the steady state analysis

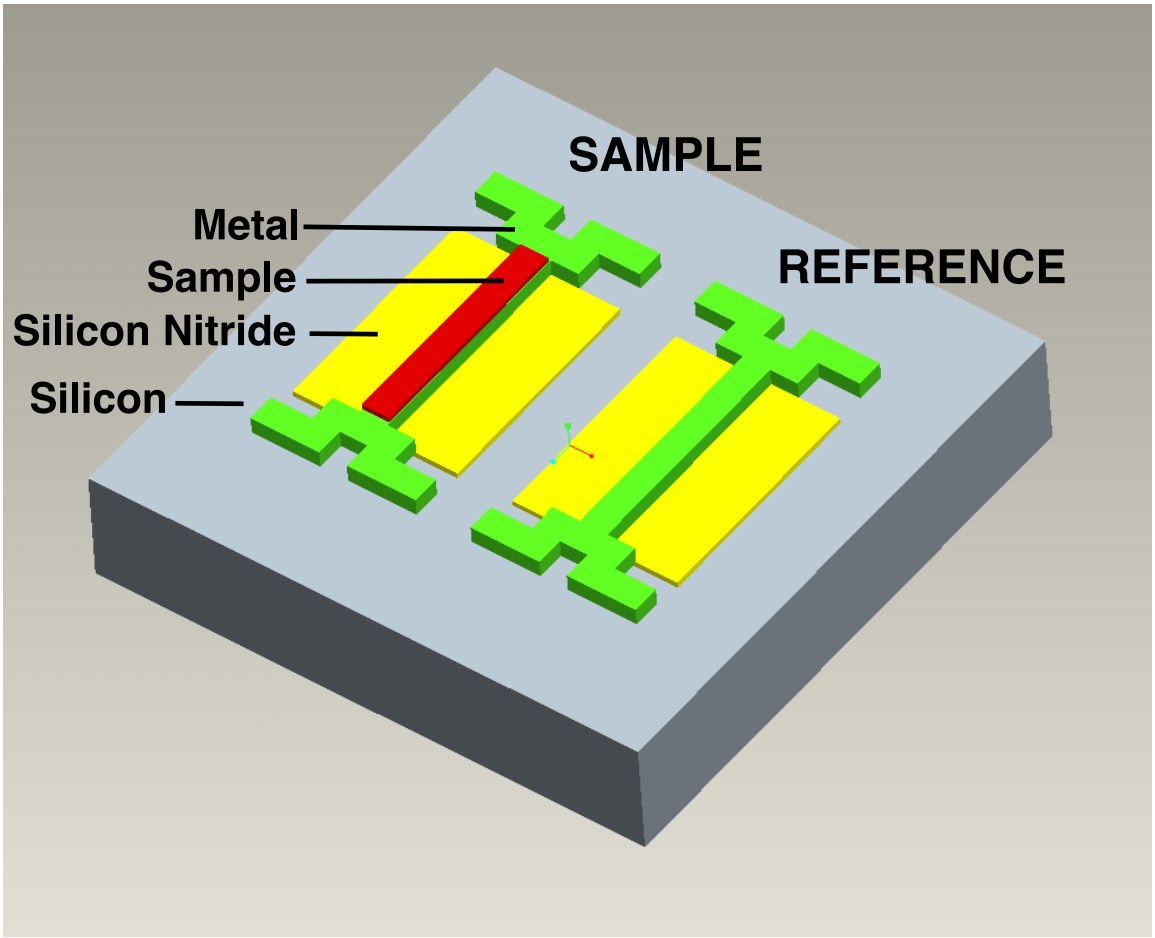

Figure 3.1: Overview of differential scanning calorimeter

resistance network can be followed through figure 3.3. Equation 3.1 takes into account all resistances displayed in figure 3.3. Ambient resistance involves heat loss by conduction to the ambient and heat loss through radiation.

$$R_{Total} = \left[\frac{1}{R_{Polymer} + R_{Ambient}} + \frac{1}{R_{SiN} + \left(\frac{1}{R_{Si} + R_{Ambient}} + \frac{1}{R_{Ambient}} \right)^{-1}} \right]^{-1} \tag{3.1}$$

Equation 3.1 neglects possible losses through interfaces. interface resistances depend on the process details of the sample deposition and bonding to the metal heater. Interface resistances can be experimentally determined for each sample by running seperate measurements. Major thermal masses involved in the device can all be

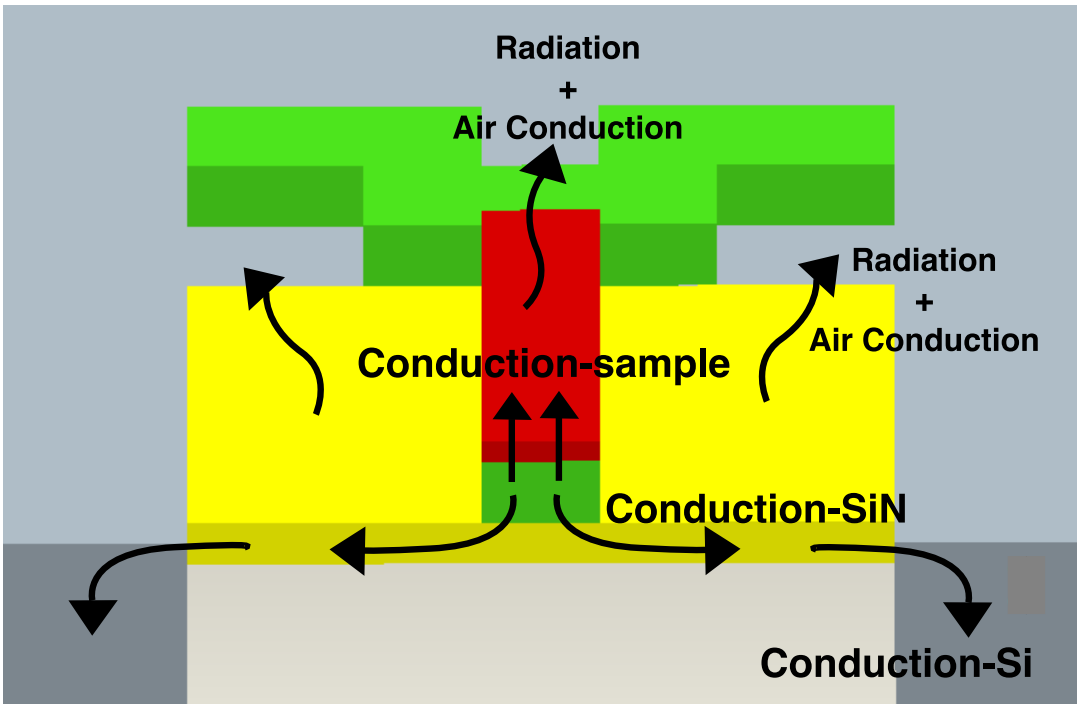

Figure 3.2: Heat dissipation path used in the thermal analysis

assessed using this equation. Resistance calculations are based on fundamental heat resistance equation:

$$R_{Thermal} = \frac{L}{kA} \tag{3.2}$$

Similarly thermal resistance due to conduction through air can be calculated using equation 3.3 [28]

$$R_{cond-air} \sim \left(\frac{1}{2k_{air}(D_{eff})}\right) \tag{3.3}$$

where effective diameter (D_{eff}) is used for modeling conduction from a circular disk to a semi infinite medium, k_air is thermal conductivity of air. Effective diameter, D_{eff} can be estimated using equation 3.4, where l and w represent the length and width of the surface.

$$D_{eff} = \sqrt{\frac{4(lw)}{\pi}} \tag{3.4}$$

Experiment is carried out in a vacuum chamber at an estimated pressure of 1.5x10^{-3}. Another important heat path is through radiation. Radiation has been

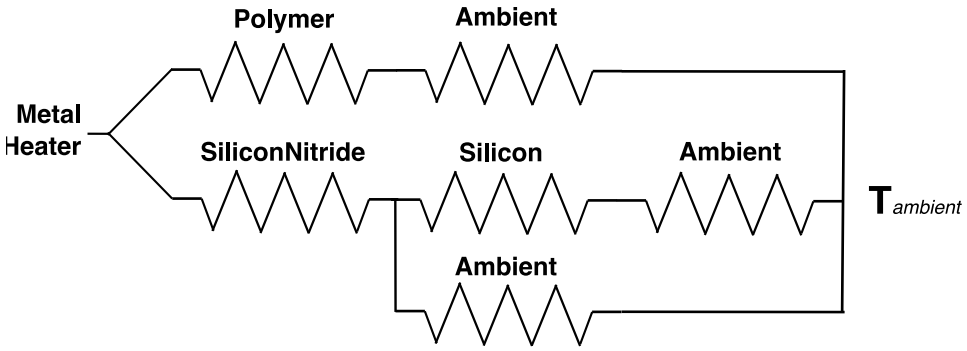

Figure 3.3: Heat flow path: simplified resistance network

included in our calculation using conservative temperature estimates for the

$$Q_{Radiation} = \varepsilon\sigma A(T^4_{surface} - T^4_{\infty}) \tag{3.5}$$

$$R = \frac{\Delta T}{\dot{Q}_{Radiation}} = \frac{\Delta T}{\varepsilon\sigma A\Delta T(T^2_S + T^2_{\infty})(T_S + T_{\infty})} \tag{3.6}$$

$$R_{radiation} \sim \left(\varepsilon\sigma(lw)(T^2_{surface} + T^2_{ambient})(T_{surface} + T_{ambient})\right)^{-1} \tag{3.7}$$

equation 3.7 uses universal Stefan-Boltzmann constant, σ and emmisivity, ϵ of the material surface. The results of above equations can be compiled in Table 3.1. Table 3.1 summarizes results of the heat flow analysis carried out using a conservative approach. The sample used for calculations is a thin polyimide layer with a thickness of 50nm. As can be seen from the table radiation effects account for less than 1% of total resistance and can be neglected for further steady state calculations. The result of resistance analysis yielded that the ratio of polymer resistance in comparison to total resistance is within a factor of 10^6 :

$$\frac{R_{Polymer}}{R_{Total}} \sim 8.2 \cdot 10^{-6} \tag{3.8}$$

this result concludes the heat flow analysis validating the design for maximum efficiency through minimization of heat dissipation on nano-calorimeter's structural

Table 3.1: Summary of thermal resistance calculations [1, 2]

	Thermal Conductivity Constant k(W/mK)	Thermal Resistance (K/W)
Polymer	$2.5x10^{-01}$	$1.03x10^{-01}$
Silicon Nitride	$3.2x10^{00}$	$1.17x10^{06}$
Silicon	$1.48x10^{02}$	$1.01x10^{01}$
Air	$3.00x10^{-02}$	$1.06x10^{04}$
Radiation	-	$2.46x10^{-05}$
R Total	-	$1.2x10^{04}$

elements. The second step in design analysis will be evaluating transient analysis and sensitivity of the device.

3.2.2 Transient Analysis

In this section details regarding transient analysis, sensitivity of the design and maximum attainable heating rate is calculated using fundamental heat transfer equations. The joule heater design requires understanding of a simple electric circuit as well as heat capacity analysis. The metal line used as a heating device is provided with a current I, and electrical resistance of the conducting wire causes release of heat. Joule heating is proportional to the current provided and resistance of the metal line as follows:

$$Power = IV = I^2R \tag{3.9}$$

where V is voltage and R is electrical resistance in ohms. The power is generated by applying a current and then power is converted into the heat domain using the:

$$\frac{dQ}{dt} = C_p\frac{dT}{dt} = I^2R \tag{3.10}$$

where Q, C_p, T, t represent heat, heat capacity, temperature, time respectively. Using results from equation 3.10 we can derive a relationship that relates the

current input to the total capacitance of the nano-calorimeter.

$$Q_{Supplied} - Q_{Loss} = Q_{net} \tag{3.11}$$

$$I^2R - \frac{\Delta T}{T_{thermal}} = C_p \frac{dT}{dt} \tag{3.12}$$

where subscript m stands for metal. Equations 3.11 and 3.12 describe the joule heating mechanism and its relationship to sample heat capacity. It is important to remember that the joule heater based thermometry measurements rely on linear change in resistivity of the metal with changing temperature. To ease transient analysis it is necessary to establish variable θ such that:

$$\theta = T_m - T_\infty \tag{3.13}$$

$$d\theta = dT_m = (T_m(t) - \cancel{T_\infty(t)}) - (T_m(0) - \cancel{T_\infty(0)}) \tag{3.14}$$

In order to understand joule heater system its essential to understand how resistivity, ρ changes with increasing temperature. Rearranging equation 3.12 yields:

$$I^2 \left[R_0 + \theta \frac{d\rho}{d\theta} \frac{L}{A} \right] - \frac{\theta}{R_{Thermal}} = \frac{d\theta}{dt} C_{metal}$$

$$I^2 R_0 + \theta \left[I^2 \frac{d\rho}{d\theta} \frac{L}{A} - \frac{1}{R_{Thermal}} \right] = \frac{d\theta}{dt} C_{metal} \tag{3.15}$$

$$\frac{I^2 R_0}{C_{metal}} + \theta \left[I^2 \frac{d\rho}{d\theta} \frac{L}{A C_{metal}} - \frac{1}{R_{Thermal} C_{metal}} \right] = \frac{d\theta}{dt}$$

$$B \qquad + \theta \, [\qquad\qquad A \qquad\qquad] = \frac{d\theta}{dt}$$

Solution for equation 3.15 is in the exponential form and can be written as:

$$\begin{aligned} \theta(t) &= Ce^{At} \\ when\ t = 0 \qquad \theta(t) &= Ce^{At} - \frac{B}{A} \end{aligned} \tag{3.16}$$

where A, can be used to derive the time constant of the system. B , can be used to compare the results of steady state temperature increase. Using results from 3.1 and handbook values for material constants it is possible to evaluate the design and given dimensions. Using dimensions given in table 3.2 and equations 3.16 and 3.15,

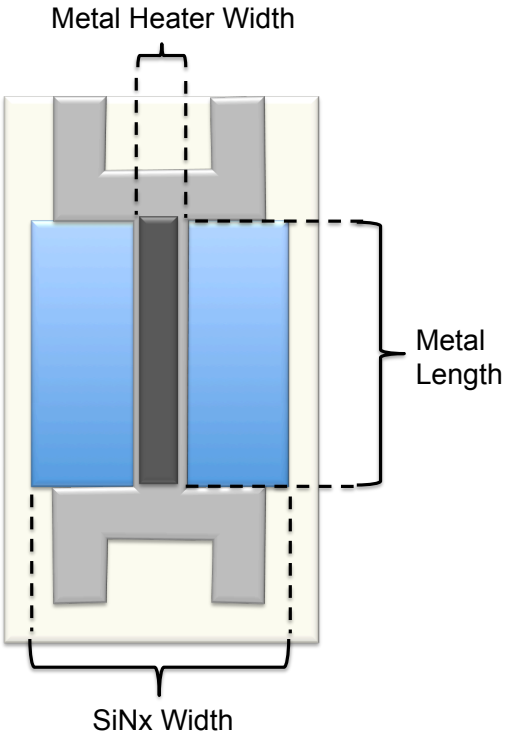

Figure 3.4: Critical dimensions of the device

we can obtain the A and B values for heating rate and time constants for each design iteration. The calculations are carried out for a 10mA current input and a deposited metal line of 50nm height. Using the results of tables 3.3 and 3.2 along with the resistance ratio between the sample and the device(Eqn 3.8) we can derive

Table 3.2: Summary of device dimensions for three different design iterations

Dimension	Design 1	Design 2	Design 3
SiN_x Width(μm)	3000	3000	3000
Metal Heater Width(μm)	500	300	150
Metal Length (μm)	3500	3500	3500

Table 3.3: Summary of calculated time constant and heating rate using transient analysis

Calculation	Design 1	Design 2	Design 3
B (K/s)	1800	5000	20000
A (s^{-1})	$4x10^2$	$5.3x10^2$	$7.5x10^2$

the sensitivity of the system based on available instruments and their sensitivity(Table 3.4). The design has been validated for use of a nanometer thick polymer film sample such as polyimide. The device sensitivity is rated at picojoule/K that stems from low thermal mass of the device(170nJ). It should be noted that sensitivity relies heavily on current resolution (2pA) and voltage resolution (1μV) of the instruments and proper calibration of the system. High sample to device resistance ratio adds to the sensitivity of the system by isolating the sample from surroundings. We can use sensitivity of the device and minimum volume capacity to calculate the minimum thickness range of the sample as follows

$$t = \left(\frac{C_p(T_S(t))}{\bar{C}_P} \right) /(l_s \cdot w_s) \tag{3.17}$$

Using equation 3.17 for polyimide ($\sim 1MJ/m^3$) with known device dimensions and minimum sensitivity (pJ), the minimum measurable thickness is found to be in the Angstrom regime.

Table 3.4: Sensitivity limits of commercial equipment used in experiment

Variable	Device Limits
Voltage	$0.1 \pm 0.003\%$
Current	$2nA \pm 0.4\% + 2pA$

CHAPTER 4

EXPERIMENT

4.1 Fabrication

Fabrication of micro-calorimetry device was carried out in University of Illinois Micro Nano Technology Labs. The facilities consists class 100 and 1000 rooms for lithographic processes. The design of the calorimetry device requires samples to be deposited on top of the device layer. The sample deposition and adhesion between metal and sample prevent us from reusing the sensor device. In order minimize fabrication time, 25 samples are all fabricated in one 4" wafer batch. Details of the fabrication steps, used tools and process details are provided using step by step instructions. The process can be visually traced using figure C.1

1. The devices are built on an n-type Si:P[100] Double side polished silicon wafer. The wafer batch used is SEMI prime 4" diameter, with a thickness of 300±25 and resistance rating of 1-15 Ωcm, made by ITME (purchased through El-Cat Inc). Before any processing wafer are cleaned using RCA. Organics can be removed using 4:1 $H_2SO_4 : H_2O_2$, for 10min at 90. Clean using Distilled Water(DI) for 5 minutes. Metal removal can be carried out using 5:1:1 $H_2O : HCl : H_2O_2$, for 10 min at 70. Clean using DI for 5 minutes. Depending on the next step a 15-30 sec HF dip can be carried out for removing native oxide and clean using DI for minutes before drying using nitrogen.

2. The first layer is deposition od Al_2O_3 on top using Atomic Layer

Deposition(ALD). ALD deposition rate is around $0.9\mathring{A}$ and we deposit around $99\mathring{A}$ using 110 cycles.

3. The second layer is deposition of the freestanding membrane. The layer can be $SiN_x or SiO_2$ depending on availability of the tools and sources. In order to measure deposition stress FSM 500TC measurement device is used. The device uses a laser system to measure the length before and after the deposition to assess residual stress. It is critical to take the initial measurement before depositing the layer and then take the second measurement after the deposition.

   (a) SiN_x deposition is carried out using STS Multiplex CVD System. The recipe uses Platen Temperature of 300(Lower Electrode) and 240 for Showerhead(Upper electrode). Chamber pressure is 900mTorr, Nitrogen flow is always set to 1960sccm. The advantage of the system relies on its capability to use multiple frequencies consecutively, this allows high compressive stress for low frequency operation to be canceled out by high tensile stress induced in the high frequency layer. For this study %20, 40sccm SiH_4, %20 50sccm NH_3 are the process gases. The RF power is set to 20W HF(13.56Mhz) for 6 seconds followed by 20W LF(380kHz) for 2 seconds, applying power on showerhead first. The deposition takes 8 minutes 48 seconds(65 cycles) and yields 131-133nm, with a residual tensile stress of 60-80MPa.

   (b) SiO_2 deposition is carried out using Kurt J Lesker PVD75 Dual Gun Sputtering System. Deposition is carried out at room temperature and pressure of 1.5mT. The power is set to 300W, and % 100 Argon gas is used during sputtering of SiO_2. The deposition rate is around 1nm/min and after 4 hour deposition 240nm layer can be obtained.

4. Next step is to prepare the wafer for deposition of metal layer. The process begins by primer HMDS spin coating at 3500rpm for 35seconds. The second step is spin coating a layer of Shipley 1813 positive photoresist(PR) at 3500rpm for 35 seconds preheating can be applied to vaporize any water eft from previous processes. Spinning is followed by baking on hotplate of 110 for 90 seconds. The PR is patterned using metal mask from D. The alignment is carried out with Quintel Q7000 IR Backside Mask Aligner. The mask is aligned using the flats for ease with following steps. The UV exposure takes 10sec(7.5mJ/cm^2) for a total of 75mJ/cm^2. The PR is devloped using AZ300MIF solution for 60seconds. Each patterning process is followed by close inspection using microscope. As seen in figure 4.1 the pattern should be free of any PR remnants, additional 5 sec development can be applied for remaining PR.

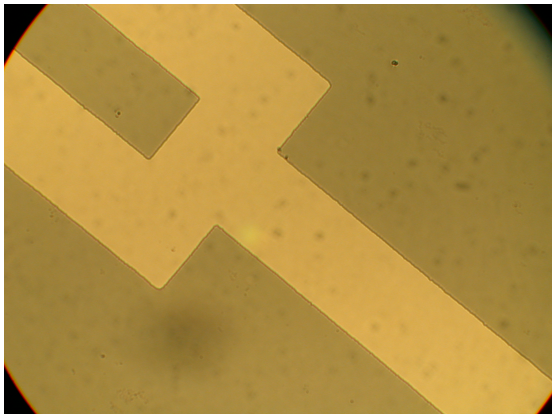

Figure 4.1: 10x microscope image of patterned layer after development of PR

5. Once patterning is complete metal layer can be deposited using CHA SEC-600 E-Beam/Thermal Evaporator. The metal layer can be chosen as Aluminum or Platinum, each metal has its own advantages for certain temperature range applications. CHA can provide high quality and uniform metal layers when used in low pressure high vacuum. On average 2 to 3 hours of pumpdown time

is required to reach a pressure level on the order of 10^{-7}. Once desired level of pressure is reached metal can be deposited using automatic or manual modes. When using manual mode it is important to use a step by step approach rising the power level slowly % 10 per minute followed by soaking period of 1min with no power increase. For Al deposition it is sufficient to rise up to % 37 power and then deposition can begin with an average rate of 1-2$\mathring{A}$/sec. Careful attention should be given to center the beam center of the source and to apply small amount of oscillation in order to avoid hot spots in the crucible. Deposition rate should be controlled to avoid high oscillations that range between 1-4$\mathring{A}$/sec. If the deposition rate has high jumps crystal can be replaced. For Pt deposition initial layer of 3nm Ti can be applied to promote adhesion and avoid liftoff issues. metal layer is deposited for a thickness of 50nm.

6. Once the metal deposition is complete the wafer should be soaked into an acetone bath and left for liftoff at least for an hour. The liftoff can take anywhere between 3hours to overnight. Pt layers take longer than aluminum. It is possible to speed up liftoff process by sonication for 20seconds. After each sonication attempt acetone should be cleaned and the sample inspected for metal remnants.

7. After initial metal deposition a second pattern is made using same procedure described in 4. The mask used for the second pattern is the metal spacer mask. This creates a secondary metal layer to act as a spacer that protects the measuring portion of the device from the carrier wafer. Upon completion of the second pattern another layer of metal is deposited using CHA SEC-600 E-Beam/Thermal Evaporator. The second layer is thicker in comparison to the initial device layer, for 50nm Al, additional spacer of 250nm is deposited.

Following deposition liftoff is done as explained in 5.

8. The next step is preparing the wafer for backside etch. Initially a layer of PR(Shipley 1813) is spin coated and immediately following the spin a second carrier wafer(DSP for backside alignement) is bonded to the surface and pressured to keep together. In order to keep wafers together they should be baked on hot-plate for 2 minutes (at 110). This step can be carried out either before or after pattering of the backside. In either case before proceeding with further steps top layer should be spin coated with PR for protecting fragile metal surfaces from scratching

9. Backside patterning uses a thick layer of PR as an ICP mask. AZ4620 is used as a masking layer for it high selectivity 54:1 and 19μm thickness.The first step is HMDS primer coating using spinner at 3500rpm for 35 seconds. The second step is to spin AZ4620, special attention should be given to avoid any air bubbles before spinning the PR. The spin is carried in incremental steps 3 seconds at 300rpm (150r/s), 20 seconds at 1800rpm (1250r/s) and lastly 120sec at 1600rpm(1800r/s) to achieve a uniform layer. Spinning will be followed by 5 minutes of resting the sample on the spinner chuck. The wafer can then be baked on a hot-plate for 5minutes at 110. The perimeter of the wafer will have a thicker layer of PR, it is possible to use a que tip with acetone to clean the thick PR around the wafer. The wafers need to sit at room temperature for at least 45 minutes before patterning. The patterning uses the window mask displayed in D. This step requires backside alignment unless the pattern was done earlier using a silicon nitride layer. After backside alignment the exposure is set to 60seconds(450mJ/cm^2). The developer used in this process is AZ400K diluted 4:1, the development time is usually 3-4 minutes and should be carefully tracked after the thrid minute. Swirling and

the size of the beaker can speed up the development process, as a precaution one should always observe the development process and check using a microscope when in doubt of overdeveloping.

10. The last process step is etching the backside using STS Mesc Multiplex Advanced Silicon Etcher. The top layer of the PR should be smoothened by 30second oxygen plasma before etching begins. ICP uses Bosch process to create a uniform walled etch. The process parameters used for deep etching using ICP (recipe 2, oks2) is as follows etch step 130sccm $SF_6 + 13sccmO_2(12 + 0)$ pressure:40mT, RF coil 600W, platen 12W. For the deposition step 78 scccm $C_4F_8(8 + 0)$, pressure 22mT, RF coil 600W, platen 0W. Platen temperature of 20 and lid temperature of 45. The recipe for slower etch rate of $1.5\mu m$ is recipe 3 (oks3). The etch step 130sccm $SF_6 + 13sccmO_2(7 + 0)$ pressure:15mT, RF coil 600W, platen 12W. For the deposition step 110 scccm $C_4F_8(5 + 0)$, pressure 10-14mT, RF coil 600W, platen 0W. Platen temperature of 20 and lid temperature of 45.

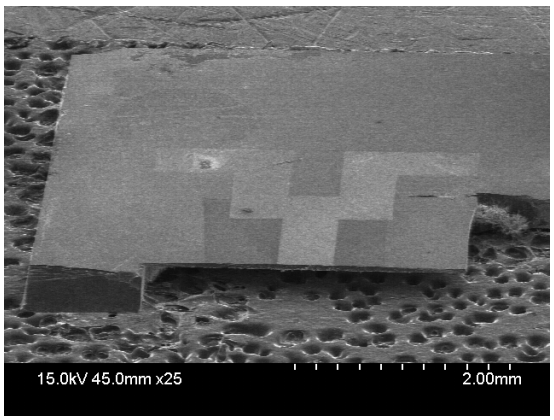

(a) SEM image of a device

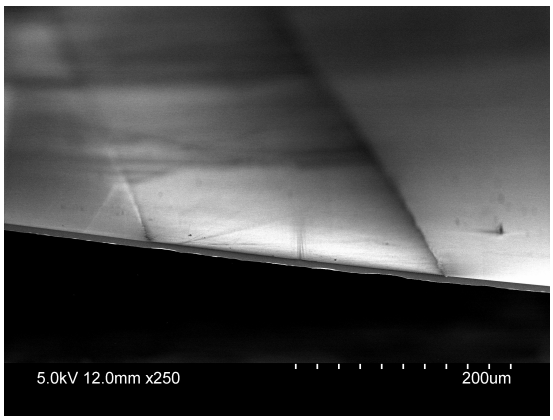

(b) SEM image of metal bridge

Figure 4.2: SEM images of the device taken by dividing at the center

4.2 Calibration

The calibration of the device is carried out using a temperature controlled vacuum chamber. Our labe setup consists of a ST-100 Cryostat along with a pumping system. The cryostat can provide an operating temperature range between 2.5K to 500K. For our application calibration needs to be carried for temperatures starting at room temperature. Along with a crysostat Lakeshore (331S) temperature controller is used to ramp the ambient temperature up to 500K. The measurement technique is also known as four point measurement to obtain resistance at each temperature. In order measure resistivity of the wire we provide a certain amount of current that is small enough such that the joule heating is negligible(the heating becomes apparent after 0.1mA).Keithley 6221 AC\DC supply is used to provide a DC current of 0.05mA magnitude and Keithley 6485 PicoAmmeter along with a Agilent 34401A Multimeter is used to measure current and voltage respectively. The resistance and resistivity is calculated using:

$$R = \frac{V}{I} \tag{4.1}$$

$$\rho = \frac{RA}{L} \tag{4.2}$$

where emphρ, resistivity can be found using known dimensions of the metal line.

Measurements are taken at 10K intervals and at each temperature point at 8-10 minutes should be waited to settle the ambient temperature. The measurements are taken at each point for two minutes and then averaged to suppress fluctuations in the data. the best calibration curves are observed when one ramps up to the highest temperature slowly (1K/min) and then holds the chamber at highest temperature for at least an hour to settle the ambient chamber temperature.The measurements taken during cool down yield more accurate results

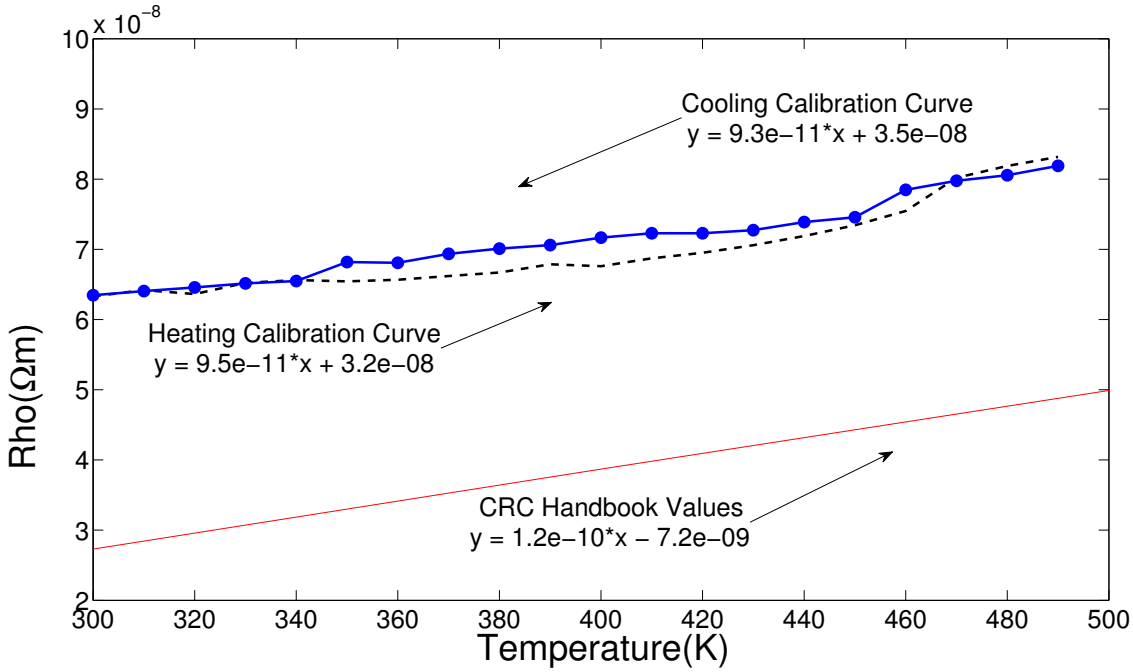

Figure 4.3: Calibration curves for Aluminum

and can help avoid non uniform temperature gradients in the chamber. All measurements are taken under vacuum, pressure being around 14-17mT. The following graphs display the calibration curve for Aluminum layer.

As displayed in figure 4.3, the calibration curve for cooling displays a more linear trend. The slope of the calibration curve is similar to handbook values and the slope differs only %22. Similar to aluminum calibration of platinum yields better linear trends for cooling in comparison to heating. The slope of the cooling curve is provided for calculating change in temperature using change in resistance.

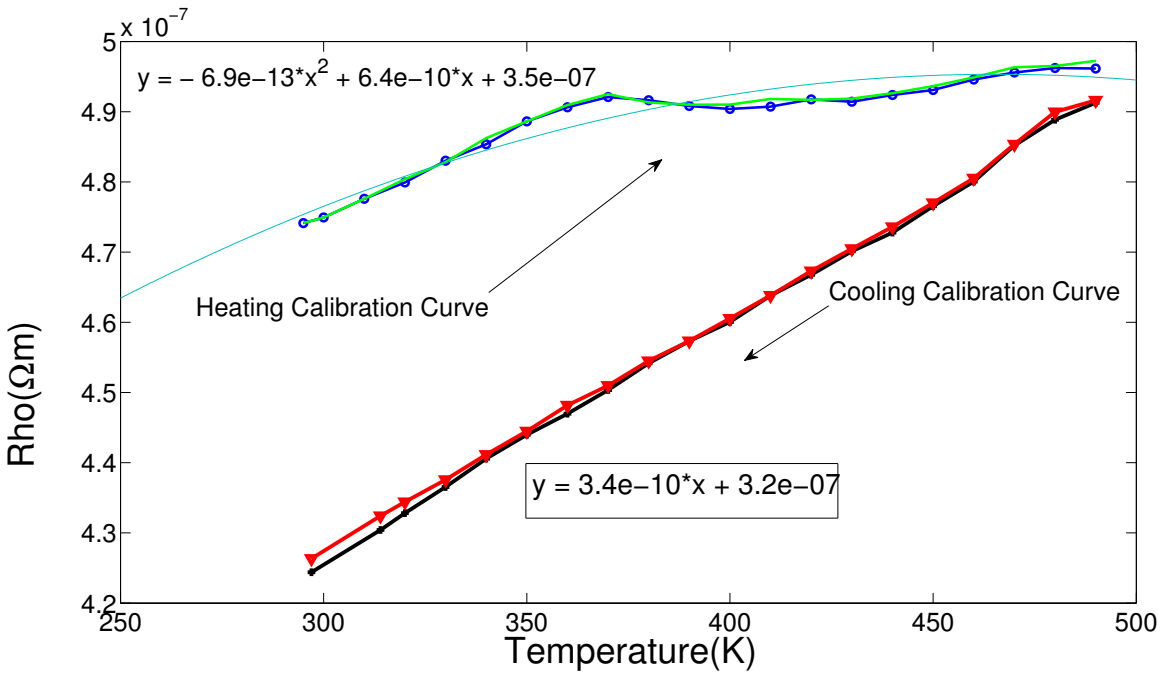

Figure 4.4: Calibration curves for Platinum

CHAPTER 5

CONCLUSIONS

5.1 Summary

Capacitive thermal management is an attractive solution for handheld devices with transient power profiles. However, the existing choices for phase change materials render such a solution infeasible at present. In this thesis, the key figure of merit for capacitive thermal management as the enthalpy change of the PCM per unit volume is identified. Using fundamental thermodynamic relations, the linear relation between enthalpy change per unit volume and the degree of superheating past the melting point is shown. The thesis also discusses that a system of nanostructures with cohesive interfaces can exhibit superheating that enhances the enthalpy change by 100 % when the nanostructure dimensions approach 10 nm.

Finally, description of a novel microfabricated calorimeter that can experimentally verify such interface driven enthalpy enhancement in thin film systems is explained in detail. Analysis of this mico-calorimetry device shows that its sensitivity approaches sub nano-Joules. Future measurements will accurately characterize nanometer scale layered thin film structures for verifying the theoretical work.

This work advances the state-of-art of phase change cooling by proposing a path toward enhancing the volumetric enthalpy for melting and hence the thermal storage capacity per unit volume.

5.2 Future Work

Capacitive thermal management can be resolved using novel material solutions that are up and coming in the research scene. The work can be expanded by investigating caged material structures such as zeolites where multiple materials with complementary physical properties can be brought together. In this aspect an alternative approach is to take advantage of intrinsically larger enthalpy associated with liquid-vapor phase transition. This change in enthalpy can be traced down to entropy change during vaporization. In order to use vaporization material needs to be encapsulated in a shell type enclosure or embedded within a porous structure. Proposed shell structure will utilize Br as core material. Bromine is liquid in room temperature and vaporizes at 332K. Vaporization of Bromine can potentially yield 1170 MJ/m^3. Encapsulation of liquid has been established on many occasions by silica encapsulation using precipitation of silica layer [29]. Similarly encapsulation of gas particles has been established using polymeric microbubbles. Bjerknes et al[30] uses albumin as shell material to trap air. In addition to encapsulation porous structures can be modified to fill the pores with phase change material. Experiments have been carried out for PCM confined in porous silicon[31, 32]. The biggest issue with phase transition of evaporating particles is thermal expansion. To avoid increased pressure and failure of the structure the hosting medium is required to have a negative thermal expansion constant. Matching two materials with similar absolute expansion coefficients in opposing directions can lead to zero expansion coefficient material composites. The system can be observed in Figure 5.1. Such structures can be achieved using metal-organic frameworks(MOFs). MOFs have high negative expansion coefficients due to their molecular structure that link octahedral $Zn_4O(CO_2)_6$ clusters using aromatic carbon ring structures. The resulting structure can offer one of the highest recorded negative coefficients 1.9%

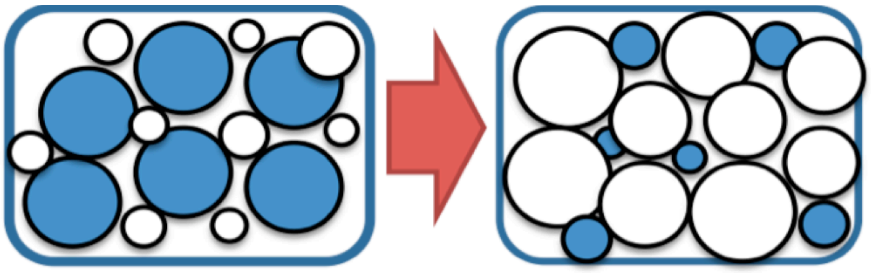

Figure 5.1: A zero thermal expansion composite with two materials of inverse thermal expansion coefficients.

for a wide temperature range of 600K. Blending such a structure with embedded polyethylene results in a zero expansion composite for temperatures between 300-600K[33]. The structure can accommodate expansion rates up to $\sim 11x10^{-6}K^{-1}$.

An alternative approach for future researchers might be using a hybrid system that can take advantage of capacitive cooling where smaller loads are encountered. A hybrid system needs to be backed up by a fan based system such that it can handle increased thermal loads without overheating.

APPENDIX A

Electromigration

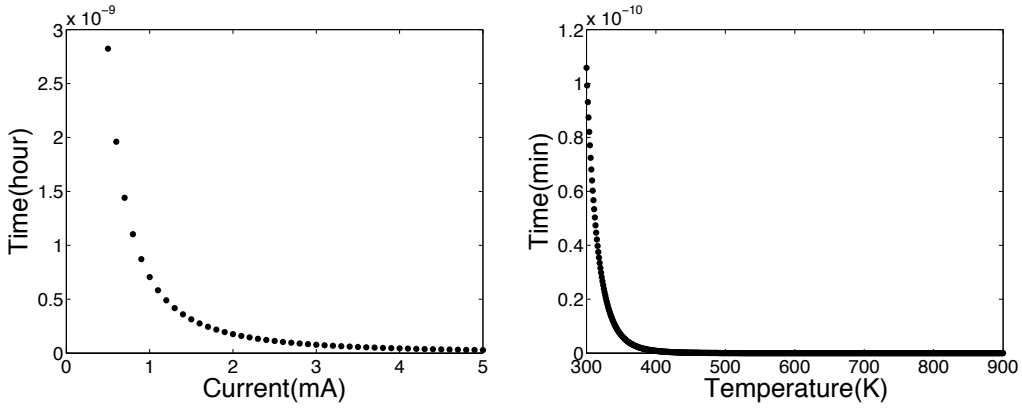

(a) Mean time to failure using 20mA current (b) Mean time to failure at room temperature

Figure A.1: MTTF - Mean Time To Failure

Electromigration is the transport of material caused by the gradual movement of the ions in a conductor due to the momentum transfer between conducting electrons and diffusing metal atoms. The mean time to failure(MTTF) can be approximated using Black's theorem. According to Black's theory:

$$MTTF = A(J^{-n})e^{\frac{E_a}{kT}} \tag{A.1}$$

where A is a geometric constant (for Al $\sim 3x10^{12}$), J is the current density. E_a is the energy barrier (for Al 0.5) and k Boltzmann's constant. Results are summarized in Figure A

APPENDIX B

Thickness Measurement:Ellipsometry

Ellipsometry is a very sensitive measurement techniques used to characterize thin film optical properties and thickness. Ellipsometry technique uses polarized light to extract optical information regarding the film and this information can be processed using software and relevant algorithms to define film properties. The sensitivity of the technique stems from determination of relative phase change in a beam of incident polarized light. The measured values are change in polarization that can be used to extract how much of the incident light is transmitted and reflected. The measured raw data is in the form of *psi,*Ψ and *del,*Δ. Psi and Del can be related to fresnel coefficient using

$$\rho = \frac{R_P}{R_S} = \tan(\Psi)e^{i\Delta} \tag{B.1}$$

Using eqn B.1 and a relevant model such as cauchy can be used to fit the data. Accurate modeling of polymers requires characterizing the layer as transparent with minimum amount of absorption in the ultraviolet spectral range. The tool used to determine thickness is Woolam spectroscopic ellipsometer, which takes measurements on a range of different wavelengths and processes them simultaneously.

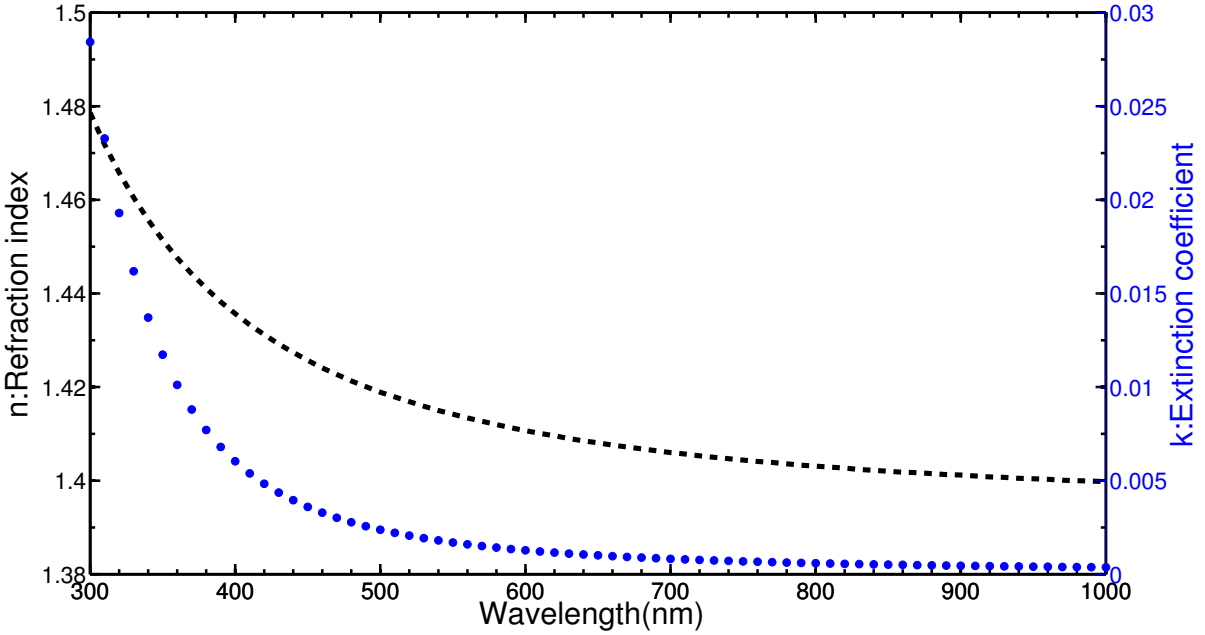

Figure B.1: Refraction Coefficient n and Extinction Coefficient k for a 60nm layer

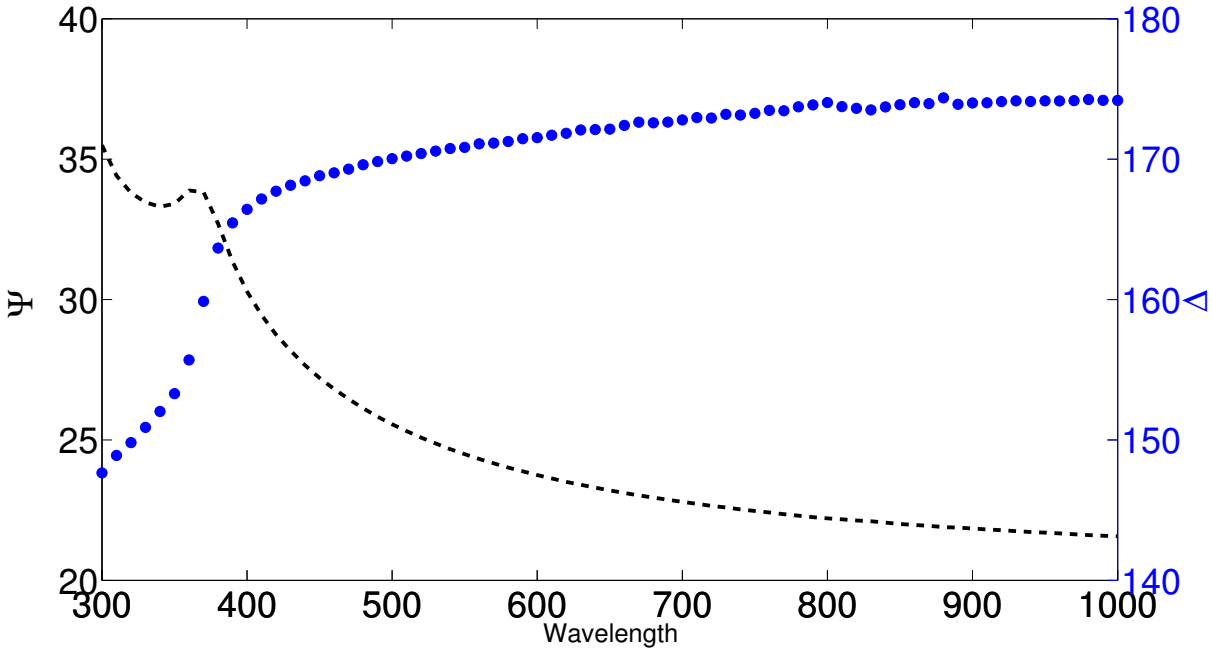

Figure B.2: Psi and Del for a 60nm layer

APPENDIX C

Process Steps

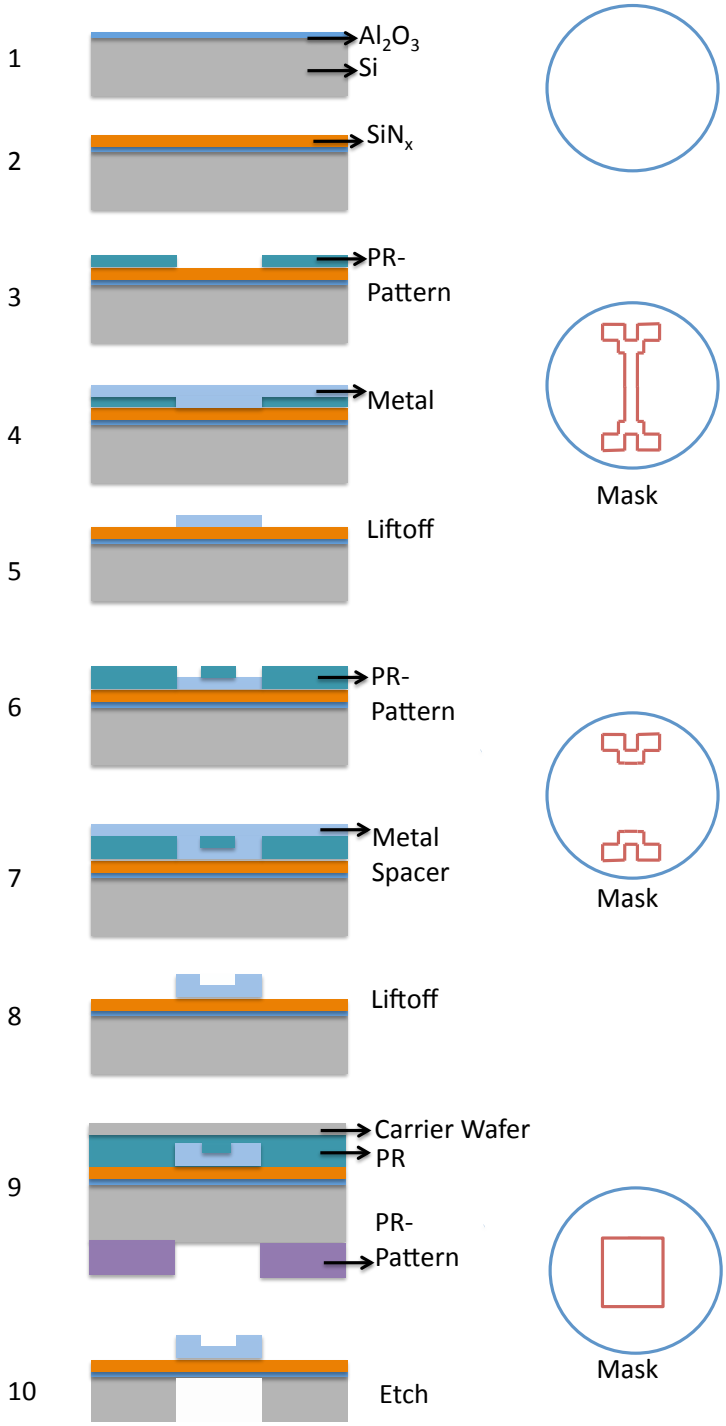

Figure C.1: Fabrication steps

APPENDIX D

Masks

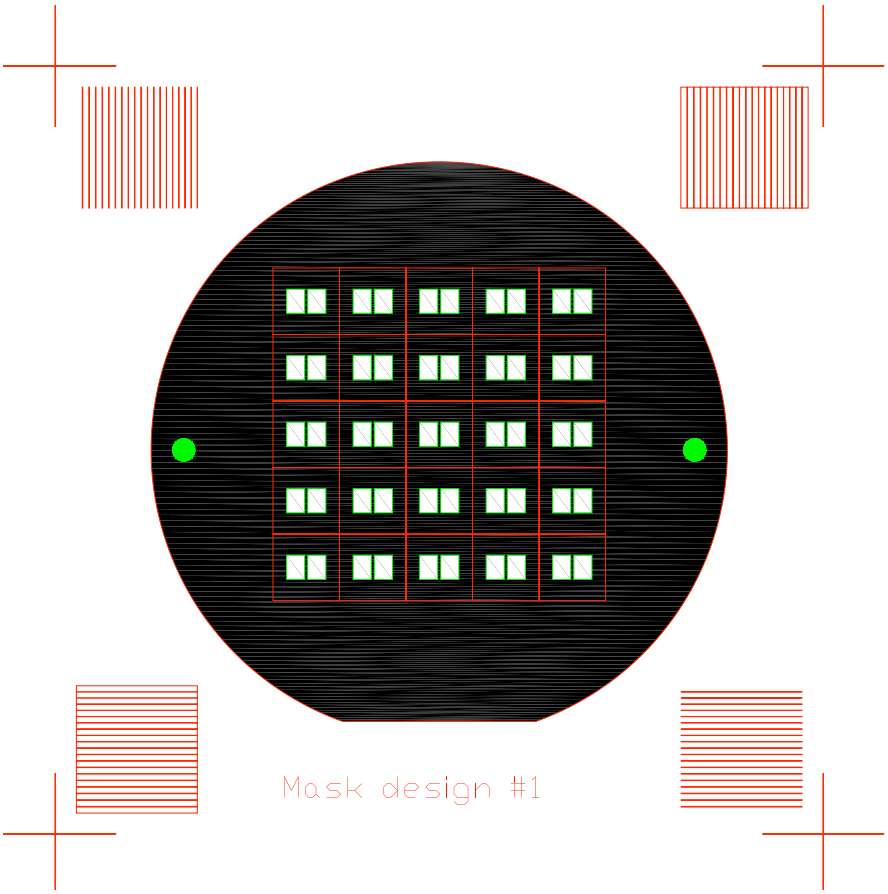

Figure D.1: Mask1

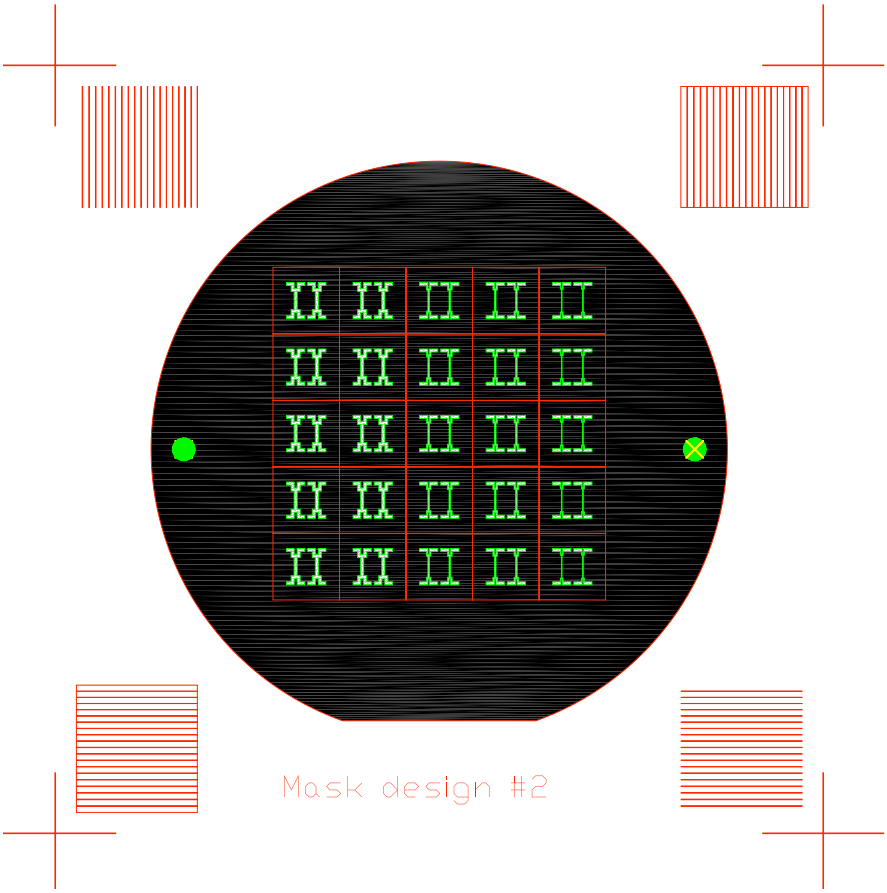

Figure D.2: Mask2

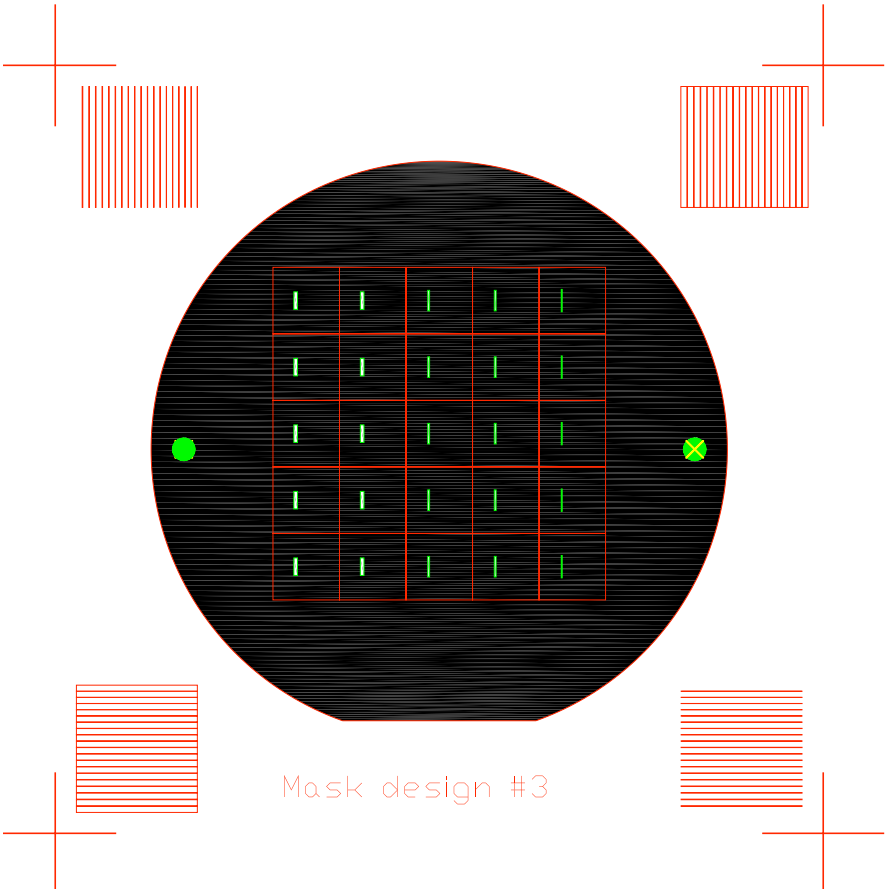

Figure D.3: Mask3

REFERENCES

[1] K. Kurabayashi, M. Asheghi, M. Touzelbaev, and K. Goodson, "Measurement of the thermal conductivity anisotropy in polyimide films," *Microelectromechanical Systems, Journal of*, vol. 8, no. 2, pp. 180–191, 1999.

[2] J. F. Shackelford, W. Alexander, and J. F. Shackelford, *CRC materials science and engineering handbook*, 2001.

[3] B. Zalba, J. M. Marn, L. F. Cabeza, and H. Mehling, "Review on thermal energy storage with phase change: materials, heat transfer analysis and applications," *Applied Thermal Engineering*, vol. 23, no. 3, pp. 251–283, Feb. 2003.

[4] A. Cosentino, "Thermal management of telecommunications batteries using phase change materials (PCM) JacketTM," in *Telecommunications Energy Conference, 2000. INTELEC. Twenlty-second International*, 2000, pp. 237–244.

[5] BASF, "Phase changing materials: intelligent temperature management for buildings." Micronal PCM product specifications sheet, 2009.

[6] H. B. Callen, *Thermodynamics*, 1960.

[7] D. W. Oxtoby, "New perspectives on freezing and melting," *Nature*, vol. 347, no. 6295, pp. 725–730, Oct. 1990.

[8] B. Wunderlich, *Macromolecular physics. Vol. 3, Crystal melting.*

[9] M. Born, "Thermodynamics of crystals and melting," *The Journal of Chemical Physics*, vol. 7, no. 8, pp. 591–603, 1939.

[10] J. E. Lennard-Jones and A. F. Devonshire, "Critical and Co-Operative phenomena. III. a theory of melting and the structure of liquids," *Proceedings of the Royal Society of London. Series A, Mathematical and Physical Sciences*, vol. 169, no. 938, pp. 317–338, Feb. 1939, ArticleType: primary_article / Full publication date: Feb. 7, 1939 / Copyright 1939 The Royal Society.

[11] F. A. Lindemann, "The calculation of molecular vibration frequencies," *Physik. Z*, vol. 11, pp. 609–612, 1910.

[12] L. H. Liang, J. C. Li, and Q. Jiang, "Superheating thermodynamics of nanocrystals based on the interface effect," *Physica B: Condensed Matter*, vol. 322, no. 1-2, pp. 188–192, Sep. 2002.

[13] K. K. Nanda, S. N. Sahu, and S. N. Behera, "Liquid-drop model for the size-dependent melting of low-dimensional systems," *Physical Review A*, vol. 66, no. 1, p. 13208, 2002.

[14] K. C. Huang, T. Wang, and J. D. Joannopoulos, "Superheating and induced melting at semiconductor interfaces," *Nature (London) Phys Rev Lett*, vol. 94, p. 175702, 1978.

[15] R. Lipowsky, "Critical surface phenomena at first-order bulk transitions," *Z. Phys. B Phys Rev Lett*, vol. 49, p. 1575, 1981.

[16] H. Elias, *Macromolecules*. Wiley-VCH, 2008.

[17] Q. S. Mei and K. Lu, "Melting and superheating of crystalline solids: from bulk to nanocrystals," *Progress in Materials Science*, vol. 52, no. 8, p. 11751262, 2007.

[18] B. Wunderlich, "One hundred years research on supercooling and superheating," *Thermochimica Acta*, vol. 461, no. 1-2, p. 413, 2007.

[19] L. Zhang, L. H. Zhang, M. L. Sui, J. Tan, and K. Lu, "Superheating and melting kinetics of confined thin films," *Acta Materialia*, vol. 54, no. 13, p. 35533560, 2006.

[20] G. G. Buchaillot, "Modeling the melting enthalpy of nanomaterials," *The journal of physical chemistry*, vol. 113, no. 9, 2009.

[21] TAInstruments, "Ta instruments microcalorimetry," TA Instruments Product Brochure, 2009.

[22] S. Early, F. Hellman, J. Marshall, and T. Geballe, "A silicon on sapphire thermometer for small sample low temperature calorimetry," *Physica B+C*, vol. 107, no. 1-3, pp. 327–328, 1981.

[23] D. W. Denlinger, E. N. Abarra, K. Allen, P. W. Rooney, M. T. Messer, S. K. Watson, and F. Hellman, "Thin film microcalorimeter for heat capacity measurements from 1.5 to 800 k," *Review of Scientific Instruments*, vol. 65, no. 4, p. 946959, 1994.

[24] S. L. Lai, G. Ramanath, L. H. Allen, P. Infante, and Z. Ma, "High-speed (10[sup 4] [degree]C/s) scanning microcalorimetry with monolayer sensitivity (J/m[sup 2])," *Applied Physics Letters*, vol. 67, no. 9, pp. 1229–1231, 1995.

[25] M. Y. Efremov, E. A. Olson, M. Zhang, S. L. Lai, F. Schiettekatte, Z. S. Zhang, and L. H. Allen, "Thin-film differential scanning nanocalorimetry: heat capacity analysis," *Thermochimica Acta*, vol. 412, no. 1-2, pp. 13–23, Mar. 2004.

[26] W. C. Fon, K. C. Schwab, J. M. Worlock, and M. L. Roukes, "Nanoscale, Phonon-Coupled calorimetry with Sub-Attojoule/Kelvin resolution," *Nano Letters*, vol. 5, no. 10, pp. 1968–1971, 2005.

[27] E. Olson, M. Efremov, M. Zhang, Z. Zhang, and L. Allen, "The design and operation of a MEMS differential scanning nanocalorimeter for high-speed heat capacity measurements of ultrathin films," *Microelectromechanical Systems, Journal of*, vol. 12, no. 3, pp. 355–364, 2003.

[28] M. Asheghi, "Thermal transport properties of silicon films," Ph.D. dissertation, Stanford University, CA, 1999.

[29] M. I. Goller and B. Vincent, "Silica encapsulation of liquid PDMS droplets," *Colloids and Surfaces A: Physicochemical and Engineering Aspects*, vol. 142, no. 2-3, p. 281285, 1998.

[30] K. Bjerknes, P. C. Sontum, G. Smistad, and I. Agerkvist, "Preparation of polymeric microbubbles: formulation studies and product characterisation," *International Journal of Pharmaceutics*, vol. 158, no. 2, p. 129136, 1997.

[31] C. Faivre, D. Bellet, and G. Dolino, "Phase transitions of fluids confined in porous silicon: A differential calorimetry investigation," *The European Physical Journal B-Condensed Matter and Complex Systems*, vol. 7, no. 1, p. 1936, 1999.

[32] D. Zhang, S. Tian, and D. Xiao, "Experimental study on the phase change behavior of phase change material confined in pores," *Solar Energy*, vol. 81, no. 5, p. 653660, 2007.

[33] S. S. Han and W. A. Goddard, "Metal-Organic frameworks provide large negative thermal expansion behavior," *Journal of Physical Chemistry C*, vol. 111, no. 42, p. 1518515191, 2007.